

# Photoacoustic tomography with a limited-aperture planar sensor and a reverberant cavity

B T Cox<sup>1</sup>, S R Arridge<sup>2</sup> and P C Beard<sup>1</sup>

<sup>1</sup> Department of Medical Physics and Bioengineering, University College London, London WC1E 6BT, UK

<sup>2</sup> Department of Computer Science, University College London, London WC1E 6BT, UK

E-mail: [bencox@mpb.ucl.ac.uk](mailto:bencox@mpb.ucl.ac.uk)

Received 9 March 2007, in final form 29 May 2007

Published 23 November 2007

Online at [stacks.iop.org/IP/23/S95](http://stacks.iop.org/IP/23/S95)

## Abstract

Biomedical photoacoustic tomography (PAT) is a soft-tissue imaging modality which combines the high spatial resolution of ultrasound (US) with the contrast and spectroscopic opportunities afforded by imaging optical absorption. Planar US arrays composed of piezoelectric or optical detector elements with small element sizes and fast acquisition times are readily available, making them an attractive option for imaging applications. An exact and efficient, FFT-based PAT reconstruction algorithm, that converts acoustic measurements recorded over a plane to a PAT image, is known. However, to capture sufficient data for an exact PAT reconstruction with a planar geometry requires an infinitely wide array. In practice it will be finite, resulting in a loss of resolution and introducing artefacts into the image. To overcome this limitation it is proposed that acoustic image sources, provided by enclosing the target in a reverberant cavity, are used to generate a periodically repeating sound field. Measurements of this periodic sound field can be used to reconstruct a PAT image exactly from measurements of reverberation made over a finite aperture. The existing FFT-based PAT reconstruction algorithm with only minor additional modifications can be used to generate the image in this case.

## 1. Introduction

In biomedical photoacoustic tomography (PAT), soft tissue is illuminated with a short pulse of monochromatic light, and the acoustic (ultrasonic) pressure pulses that are emitted from the regions in which the light is absorbed are detected at the tissue surface. By recording these ultrasonic waves over an array of receivers, or with a single, scanned detector, the initial distribution of the acoustic pressure can be estimated. The image of the initial pressure distribution, which is proportional to the absorbed energy density, is called a photoacoustic or optoacoustic image. Image reconstruction in PAT may be considered an inverse source problem in the sense that the initial pressure distribution acts as a source term in the associated

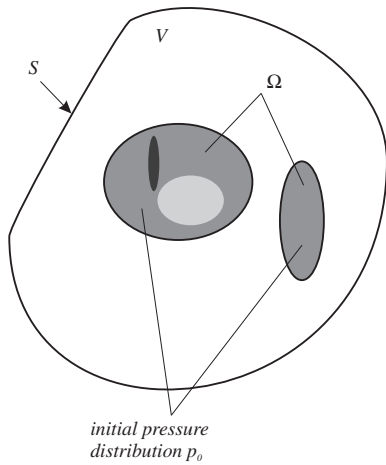


**Figure 1.** In photoacoustic tomography, acoustic time histories are measured on all or part of the surface  $S$  which surrounds the region  $V$  containing  $\Omega$ , within which the source, the initial pressure distribution,  $p_0$ , has compact support.

forward or direct problem. When the excitation light is replaced by microwave or RF radiation the technique is called thermoacoustic tomography. PAT has been used successfully in a variety of applications, including imaging of vasculature [1–3], visualization of breast tumours [4, 5] and functional brain imaging in small animals [6].

The forward and inverse (imaging) problems of PAT are described briefly below. This paper is concerned principally with image reconstruction from measurements made over a planar measurement surface. Section 2 contains a description of both the continuous and discrete forms of a well-known PAT image reconstruction algorithm for use with measurements recorded over a plane. It is shown that using acoustic pressure measurements recorded over a planar measurement surface that is finite in extent leads to image artefacts: the ‘finite aperture’ problem. Section 3 introduces the central idea in this paper: a PAT image with considerably reduced image artefacts can be formed from measurements of the reverberant field between two parallel acoustic reflectors via the discrete image reconstruction algorithm of section 2, without having to modify it significantly. In effect, using reverberant data in the reconstruction is equivalent to recording data over a larger measurement aperture. In section 4 a theorem of Louis and Quinto [7] concerning stably reconstructable boundaries within an image is used to examine the concept of an ‘effective measurement aperture’. The paper concludes with a discussion of the advantages of this technique over conventional methods of measurement and reconstruction in PAT.

### 1.1. Forward problem

Let  $V$  be the domain with boundary  $S$  in which the acoustic field propagates, and let  $\Omega \subset V$  be the support of non-zero optical absorption (figure 1). When (a) the tissue behaves as a stationary fluid with isotropic acoustic properties, (b) viscosity and thermal conductivity are negligible, (c) the sound generation mechanism is thermoelastic, and (d) the linear acoustic approximation holds, the acoustic pressure,  $p(\mathbf{x}, t)$ ,  $\mathbf{x} \in V$ , obeys the scalar wave equation

$$\left( \nabla^2 - \frac{1}{c^2} \frac{\partial^2}{\partial t^2} \right) p = \frac{-\beta}{C_p} \frac{\partial \mathcal{H}}{\partial t}, \quad (1)$$

where  $c$  is the sound speed,  $\beta$  is the volume thermal expansivity, and  $C_p$  is the specific heat capacity, all assumed constant in  $V$ . The absorbed optical energy density,  $\mathcal{H} = \mu_a \Phi$ , is the heat energy deposited in the tissue per unit volume and per unit time, where  $\mu_a$  is the optical absorption coefficient and  $\Phi$  is the fluence rate. The propagation of light in an absorbing and scattering medium is a complicated, diffusion-like process, and  $\Phi$  depends on the distribution of scattering and absorption within  $V$ , as well as the light sources. However, the distribution of  $\Phi$  is not directly relevant to the results in this paper, which is concerned only with recovering the initial pressure distribution, and not with taking the further step to recover  $\mu_a$  or  $\Phi$  [8, 9].

When the excitation light pulse is sufficiently short that the density of the tissue may be considered constant over its duration (sometimes called *stress confinement*), then the time dependence of the excitation may be modelled as a  $\delta$  function,  $\mathcal{H}(\mathbf{x}, t) = H(\mathbf{x})\delta(t)$ , and the forward model can be recast as the initial value problem

$$\left( \nabla^2 - \frac{1}{c^2} \frac{\partial^2}{\partial t^2} \right) p = 0 \quad (2)$$

$$p|_{t=0} \equiv p_0(\mathbf{x}) \quad \left. \frac{\partial p}{\partial t} \right|_{t=0} = 0. \quad (3)$$

Under this isochoric condition, the increase in the temperature  $T'(\mathbf{x})$ ,  $\mathbf{x} \in \Omega$ , is given by  $T' = H/(\rho C_v)$ , where  $C_v$  is the constant-volume specific heat capacity and  $\rho$  the ambient mass density. The thermodynamic relation  $\rho' = \rho\kappa_T p' - \beta\rho T'$ , where  $\rho'$  and  $p'$  are perturbations in density and pressure respectively, is true for constant isothermal compressibility  $\kappa_T$  and volume thermal expansivity  $\beta$ . As there is no change in the density,  $\rho' = 0$  and  $p' = (\beta/\kappa_T)T'$ . As  $\kappa_T = \gamma/\rho c^2$ , where  $\gamma$  is the ratio of specific heats, the increase in pressure due to the absorption of the laser pulse, the initial pressure distribution  $p_0$ , may be written as

$$p_0 = \left( \frac{\beta c^2}{C_p} \right) H = \Gamma H \quad (4)$$

$\Gamma$  is called the Grüneisen coefficient.

### 1.2. Inverse problem

The aim in PAT is to recover  $p_0(\mathbf{x})$ ,  $\mathbf{x} \in V$ , from acoustic pressure time histories,  $p(\mathbf{x}_s, t)$ , measured at points on the boundary,  $\mathbf{x}_s \in S$ . As the mean value of the time-integrated pressure time history recorded up to time  $t$  at  $\mathbf{x}_s$  is equal to the mean value of the initial pressure distribution on the sphere with radius  $ct$  centred at  $\mathbf{x}_s$ ,

$$\frac{1}{t} \int_0^t p(\mathbf{x}_s, t') dt' = \frac{1}{4\pi(ct)^2} \int_A p_0(\mathbf{x}) dA, \quad (5)$$

where the spherical surfaces  $A$  are given by  $|\mathbf{x}_s - \mathbf{x}| = ct$  with area  $4\pi(ct)^2$ , the reconstruction problem is one of recovering a function from its mean values on spherical shells of radius  $ct$  centred on  $\mathbf{x}_s$ . Closed form reconstruction algorithms have been devised for measurement surfaces with spherical [10–13], cylindrical [10, 14, 15] and planar geometries [10, 16, 17]. Image reconstruction based on a numerical model, which can thus accommodate a measurement surface with arbitrary geometry, has also been proposed [18]. In addition to these, a number of other methods of reconstruction have been investigated [19–30].

## 2. Image reconstruction from planar measurements

A planar measurement geometry is considered here because, as well as the practical experimental advantages that a flat measurement surface offers, planar US arrays composed

of piezoelectric or optical elements [31] with small element sizes and fast acquisition times are readily available, and, most importantly, an exact and efficient reconstruction algorithm is known for this case. There is a fundamental difference between measurements made over spherical and planar surfaces. When the measurement surface surrounds the source region, all the emitted acoustic waves are recorded. However, for a single planar measurement surface—even if infinite in extent—at most half of the acoustic emissions can be measured. Nevertheless it is still possible, in principle, to recover  $p_0$  as there is a two-fold data redundancy in PA imaging: the sources generate two sets of waves travelling in opposite directions [32].

The problem with a planar geometry is that in practice the measurements are restricted to a finite region of the infinite plane which, when using a reconstruction algorithm which assumes an infinite plane, leads to artefacts in the image. This paper proposes a method of overcoming this ‘finite aperture’ problem, by reflecting the acoustic field back onto the finite measurement surface. It is shown, in section 3, that an image may be reconstructed from this reverberant data using an existing image reconstruction algorithm, described below, which was originally derived for the case of an infinite measurement surface.

### 2.1. Reconstruction algorithm: continuous

The reconstruction algorithm used in this paper, and similar frequency–wavenumber schemes for measurements made on a plane, appear in the literature on inverse scattering problems, such as seismic migration [33, 34], ultrasound imaging [10, 35] and synthetic aperture radar [36], as well as in the mathematical literature on reconstructing a function from spherical averages [37, 38]. It was first described explicitly for PAT by Köstli *et al* [16] and more recently by Xu *et al* [17]. A 2D version [39] is briefly described below but as the method is based on Cartesian  $k$ -space it may be extended quite simply to 3D. First, an infinite and continuous planar measurement surface is considered, then the continuous solution is discretized to obtain a practical reconstruction routine.

If  $p_0(x, z) = 0$  for  $z \leq 0$  then  $p_0$  for  $z > 0$  may be recovered from  $p(x, t)$ ,  $t \geq 0$ , measured on the plane  $z = 0$ , in three steps:

- (1) Fourier transform  $p(x, t)$  from the spatial variable  $x$  to wavenumber  $k_x$ , and from the time  $t$  to the frequency  $\omega$  domain. With no loss of generalization,  $p$ , which is real, can be assumed to be even in  $t$ , resulting in a transformed function,  $P$ , that is even in  $\omega$ :

$$P(k_x, \omega) = \int_{-\infty}^{\infty} \int_{-\infty}^{\infty} p(x, t) e^{-ik_x x} e^{i\omega t} dx dt. \quad (6)$$

- (2) Map  $P(k_x, \omega)$  to  $P_0(k_x, k_z)$  for real  $k_z$ , where  $k_z$  is the spatial wavenumber in the  $z$  direction and is given by the dispersion relation

$$k_z = \text{sgn}(\omega) \sqrt{(\omega/c)^2 - k_x^2}, \quad (7)$$

where  $\text{sgn}(\omega) = 1$  for  $\omega \geq 1$  and  $-1$  otherwise. Multiply by  $c^2 |k_z/\omega|$  to get

$$P_0(k_x, k_z) = \left| \frac{ck_z}{\sqrt{k_x^2 + k_z^2}} \right| P(k_x, c \text{sgn}(k_z) \sqrt{k_x^2 + k_z^2}). \quad (8)$$

- (3) Inverse Fourier transform  $P_0(k_x, k_z)$ , even in  $k_z$ , to obtain the initial pressure distribution,  $p_0(x, z)$ , real and even in  $z$ :

$$p_0(x, z) = \frac{1}{(2\pi)^2} \int_{-\infty}^{\infty} \int_{-\infty}^{\infty} P_0(k_x, k_z) e^{i(k_x x + k_z z)} dk_x dk_z. \quad (9)$$

Only  $p_0(x, z)$  for  $z > 0$  represents the true initial pressure distribution; the half of the image for which  $z < 0$  is a reflection about  $z = 0$  which arises from the symmetries assumed above [16, 40]. This algorithm inverts the radiating part of the acoustic field, measured on the plane  $z = 0$ , to obtain the initial pressure distribution  $p_0(x, z)$ . The evanescent wave components are implicitly rejected in step two by considering only real  $k_z$ . Effectively, mapping the data from time to depth,  $t$  to  $z$ , and using an FFT to calculate the Fourier transform, makes this algorithm very efficient.

## 2.2. Reconstruction algorithm: discrete

By substituting discrete for continuous variables and sampled for continuous functions in equations (6)–(9), a discrete version of the reconstruction formula above can be obtained. The sampled functions are related to their continuous counterparts as follows:

$$p_{nm} \equiv p(x, t)|_{x=n\Delta x, t=m\Delta t} \quad (10)$$

for sample spacings  $\Delta x$  and  $\Delta t$ , and where  $n = 0, \dots, N - 1$  and  $m = -M/2, \dots, M/2 - 1$ , as time  $t = 0$  corresponds to the  $(M/2 + 1)$ th sample (for simplicity  $M$  is assumed to be an even number). Similarly  $p_{0nm} \equiv p_0(n\Delta x, m\Delta z)$ ,  $P_{kl} \equiv P(k\Delta k_x, l\Delta \omega)$  and  $P_{0kq} \equiv P_0(k\Delta k_x, q\Delta k_z)$  for  $k = -N/2, \dots, N/2 - 1$  and  $l = q = -M/2, \dots, M/2 - 1$ . The discrete versions of equations (6)–(9) may then be written as

$$P_{kl} = \text{FFT}\{p_{nm}\} \quad (11)$$

$$\hat{l}_{kq} = \text{sgn}(q) \text{ round } \{\sqrt{q^2 + a^2 k^2}\}, \quad a = cM\Delta t / N\Delta x \quad (12)$$

$$P_{0kq} = A_{kq} P_{k\hat{l}_{kq}}, \quad A_{kq} = |cq/\hat{l}_{kq}|. \quad (13)$$

$$p_{0nm} = \text{IFFT}\{P_{0kq}\}. \quad (14)$$

The usual care must be taken to ensure that the wavenumber components calculated by the FFT routine are ordered correctly, with the component corresponding to zero wavenumber in the centre. Equations (12) and (13) were obtained by using the relations  $\Delta k_x \Delta x = 2\pi/N$  and  $\Delta \omega \Delta t = 2\pi/M$ , and by setting  $\Delta z = c\Delta t$  and  $\Delta k_z \Delta z = 2\pi/M$ .

Note that, because of the interpolation error introduced in equation (12),  $p_{0nm}$  will have a small non-zero imaginary component, whereas  $p_0(x, t)$  is real. However, only  $\Re\{p_{0nm}\}$  for  $m = 0, \dots, M/2 - 1$  corresponds to the initial pressure distribution  $p_0(x, z)$ ,  $z > 0$ .

## 2.3. Example using a finite aperture and no image sources

Pressure time histories, figure 2(B), were simulated from the 2D initial pressure distribution shown in figure 2(A) for an array of detectors positioned along the line  $z = 0$ . These forward calculations were performed using a  $k$ -space model [41, 42], on a  $512 \times 512$  pixel, square grid corresponding to  $10 \text{ mm} \times 10 \text{ mm}$ , or spatial steps of  $39 \mu\text{m}$ , in 5000 time steps of 7.8 ns, corresponding to a Nyquist frequency of about 64 MHz. An initial pressure distribution consisting of regularly spaced circular sources was chosen to demonstrate how the quality of the recovered image varies with position. This source distribution was smoothed to ensure no frequencies greater than the Nyquist frequency were included in the simulated data. Gaussian noise was added to the simulated pressure data at a signal-to-noise ratio of 30 dB.

The discrete reconstruction algorithm described in section 2.2 was used to form an image. First, the pressure time histories  $p_{nm}$ , shown in figure 2(B), were Fourier transformed to give

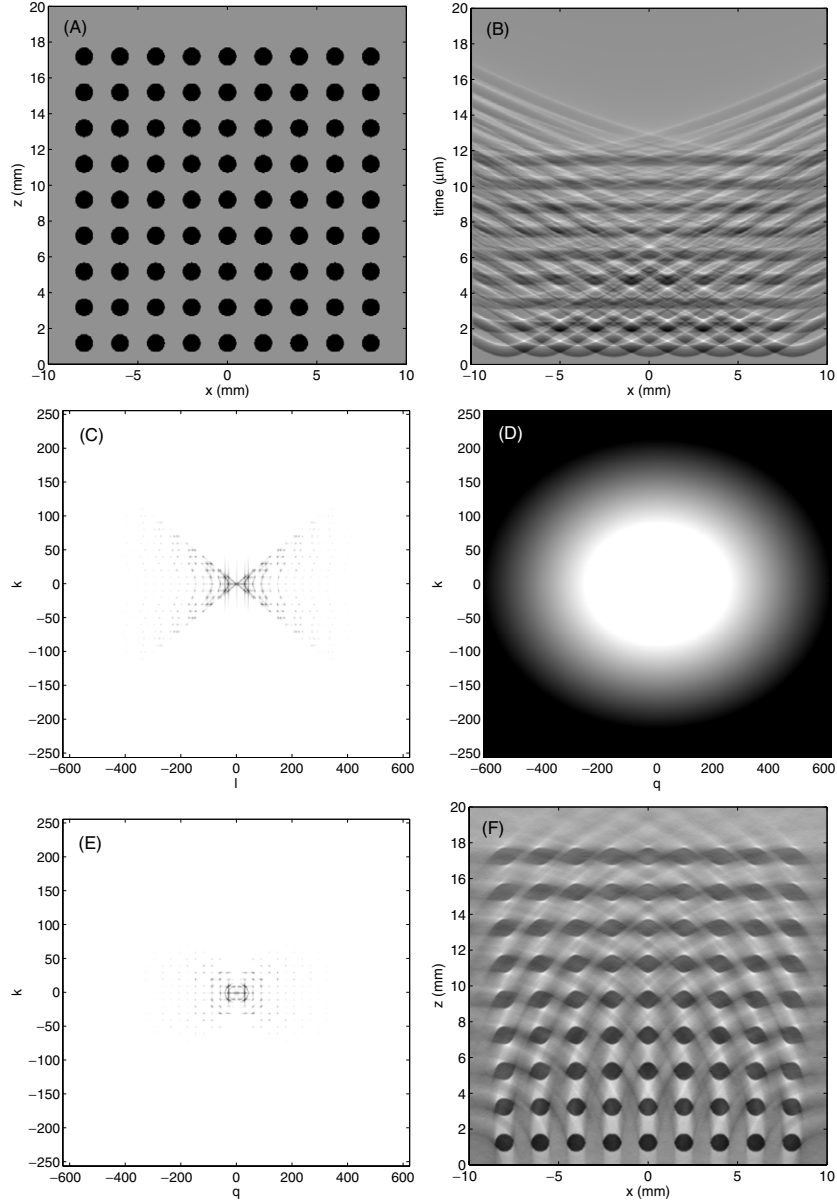


**Figure 2.** (A) The true initial pressure distribution, used to simulate (B) the pressure time histories,  $p_{nm}$ , for an array of detectors along the line  $z = 0$ , for a 20 mm aperture,  $-10 \text{ mm} \leqslant x < 10 \text{ mm}$ , in space and time steps of  $39 \mu\text{m}$  and  $31 \text{ ns}$ , respectively. (C) The Fourier transformed pressure data,  $P_{kl}$ , on a log scale. (D) The discrete frequency index  $l_{kq}$  as a function of the horizontal and vertical wavenumber indices  $k$  and  $q$ , used to map from (C),  $P_{kl}$ , to (E),  $P_{0kq}$ . (F) The estimate of the initial pressure distribution reconstructed from the finite-aperture data,  $p_{0nm}$ . The distortion and blurring introduced by the finite aperture is evident. The quality of the reconstruction decreases with distance from the centre of the detector array.

$P_{kl}$ , figure 2(C). Then  $P_{0kq}$ , figure 2(E), was estimated, using nearest-neighbour interpolation, from  $P_{kl}$  using  $l_{kq}$  as given by equation (12) and shown in figure 2(D). Finally  $P_{0kq}$  was

inverse Fourier transformed to give an estimate of the initial pressure distribution, figure 2(F). Comparing the recovered image, figure 2(F), with the true distribution, figure 2(A), shows that the features closest to the centre of the detection surface were recovered accurately. However, the distortion and blurring of the image increases quickly the further one moves from the centre of the detector plane, particularly in the direction of increasing  $z$ . The circles in the top line, about 17 mm from the detector plane, are almost blurred together in the reconstructed image, despite there being 1 mm gaps between them. The image resolution is strongly dependent on the distance from the detector and also, but to a lesser extent, on the distance from  $x = 0$ , in this finite aperture case.

### 3. Reverberant field photoacoustic tomography

#### 3.1. Acoustic reflectors

One of the limitations of using a planar sensor array is its finite measurement aperture. While a spherical detection surface can measure over a solid angle of  $4\pi$  steradians, and the infinite planar sensor over  $2\pi$  steradians (still sufficient to reconstruct an exact image), any planar sensor with a *finite* aperture is limited to solid angles somewhat smaller than this, often 1 steradian or less. By increasing the width of the aperture, and thus capturing more data, the image can be improved. However, measuring over large planar apertures soon becomes impractical due to the increasing technical complexity and prohibitive cost of very large arrays. For measurement surfaces that, to a greater or lesser extent, surround the source, such as a spherical measurement surface, the effect of this finite aperture problem can be reduced. However, the efficiency and accuracy of the FFT reconstruction algorithm may then be lost.

An image reconstructed from limited-aperture data may contain artefacts, and sharp boundaries may be blurred, as is clear from figure 2. More specifically, only boundaries where the normal to the boundary crosses the measurement surface can be reconstructed accurately [7, 43] which means that, for a small aperture, many of the boundaries in the image, especially those perpendicular to the measurement surface, become indistinct. This paper proposes placing acoustic reflectors at either end of, and perpendicular to, the measurement aperture so that the acoustic waves that would not have been recorded with just the finite aperture, i.e. acoustic rays that would have missed the sensor, are recorded as reverberation. The image reconstructed from this reverberant field contains fewer artefacts because more of the acoustic data have been used in the reconstruction. The reflectors act to extend the aperture width beyond the size of the sensor to an ‘effective’ aperture which depends on the duration of the measurement. It is shown, using examples, that boundaries within the image whose normals cross this ‘effective measurement aperture’ can be reconstructed well. A preliminary account of this approach is given in [44].

In this paper it is assumed that the reflectors are perfectly reflecting with the modulus of the reflection coefficient  $|R| = 1$ . If the acoustic waves are propagating in water ( $c = 1500 \text{ m s}^{-1}$ ,  $\rho = 1000 \text{ kg m}^{-3}$ ), then a dense material with a fast sound speed, such as steel with a normal incidence reflection coefficient of 0.94, would be required in practice. An alternative might be silica (glass) with  $|R| = 0.8$ , which has the advantage of being optically transparent, thereby allowing the excitation light through to the sample to be imaged. Optical transparency is not an essential requirement of the reflectors, as the sample may be illuminated from above, or even through the sensor in some cases, but it allows greater flexibility in the illumination geometry. Plastics such as PMMA, with  $|R| \approx 0.4$ , may not be sufficiently reflecting for this application. In principle, a pressure release boundary, where the acoustic pressure is always zero and  $R = -1$  (such as that faced by a water-borne wave reaching a

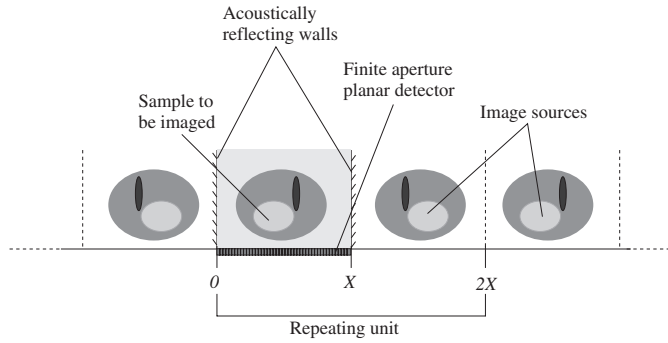


**Figure 3.** Schematic diagram of the arrangement of the planar sensor array and acoustic reflectors, showing the first few image sources. With the image sources, the effective source distribution becomes infinitely wide and repeats every  $2X$ , where  $X$  is the distance between the reflectors.

water-air interface), could be used with only minor adjustments to the theory, but this will present a greater engineering challenge than using a solid boundary.

### 3.2. Periodicity and image sources

The discrete reconstruction algorithm given by equations (11)–(14) implicitly assumes the periodicity of  $p_{0nm}$  through the use of the FFT. It is well known that a discrete Fourier transform assumes that the data to be transformed are part of a periodic function. Or, to put it the other way, transforming a function given at only discrete wavenumbers, e.g. a line spectrum such as  $P_k = P(k\Delta k_x)$  for  $k \in \mathbb{Z}$ , implicitly assumes that the resulting function, in this case  $p(x)$ , is ever-repeating, such that  $p(x + jX) = p(x), \forall j \in \mathbb{Z}$ . As the true initial pressure distribution is rarely periodic—and so the measured acoustic time histories do not originate from a periodic source distribution—the discrete estimate of that source distribution,  $p_{0np}$ , will be distorted. The origin of the distortion can be traced back to the measured data,  $p_{nm}$ , from which  $P_{0kq}$  is estimated.  $p_{nm}$  includes the sound that has travelled from the initial pressure distribution,  $p_0(x, z)$ , but does not include the sound from the infinite number of repeating replicas  $p(x + jX, z)$ ,  $j \neq 0$ , which would appear if it were periodic but actually do not exist. The underlying problem is that the measured  $p(x)$  is not part of a periodic function, and originates from a non-periodic distribution  $p_0(x)$ .

To visualize the effect of the reflectors on the acoustic field, consider the acoustic image sources they introduce. As there are two parallel and perfectly reflecting reflectors, the number of image sources is infinite and the acoustic field may be considered as infinitely repeating with a period of twice the distance between the reflectors, thereby fulfilling the requirement for a periodic function. This is shown schematically in figure 3. The data  $p(x)$  measured from  $0 \leq x < X$  can be mirrored to give a repeating function  $\hat{p}(x)$

$$\hat{p}(x) = \begin{cases} p(x) & 0 \leq x < X \\ p(2X - x) & X \leq x < 2X \end{cases} \quad (15)$$

which repeats every  $2X$ , so that  $\hat{p}(x) = \hat{p}(x + j2X), \forall j \in \mathbb{Z}$ . The same reconstruction algorithm as described in section 2 can be used to reconstruct an image from these reverberant data, giving this method the twin advantages of greater capture angle ('effective' aperture width) and efficient reconstruction. The essential point is that the reconstruction algorithm implicitly assumes that the acoustic source to be reconstructed is periodic; here it is made

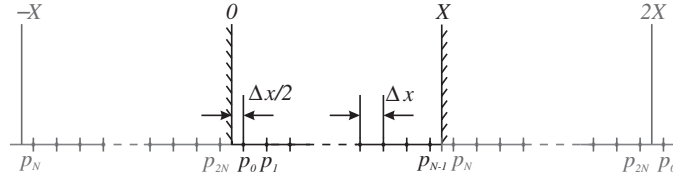


**Figure 4.** The pressure must be sampled at  $(2n + 1)\Delta x/2$ ,  $n = 0, \dots, N - 1$ , and then mirrored about the reflector at  $X$  to obtain the repeating sequence of length  $2N$  with period  $2X$ . The points, between the reflectors, at which measurements are made are shown in black.

periodic through the use of reflectors and the resulting image sources. The image quality improves because more information about the source distribution has been captured by recording over a longer time, rather than a larger aperture.

### 3.3. Sampling

It is necessary to consider the requirements on the sampling of the discrete data. There are two separate points in this section, the first general and the second specific to the measurement geometry with acoustic reflectors.

The sampling theorem states that the discrete function  $p_{0nm}$  represents its continuous counterpart  $p_0(x, z)$  uniquely if  $p_0(x, z)$  contains no spatial frequency components higher than half the spatial sampling frequency (the spatial Nyquist wavenumber). In the time domain, an analogue anti-aliasing filter is used to attenuate components at frequencies greater than half the sampling frequency. In an analogous way, components at high spatial wavenumbers can be attenuated by using a sensor that is insensitive to wavenumbers above the spatial Nyquist wavenumber. The wavenumber response of a circular pressure sensor can be approximated by  $2J_1(k_x a)/k_x a$ , where  $a$  is the radius of the sensitive element, and  $J_1$  is a Bessel function. The wavenumber components above about  $k_x(\text{max. measured}) \approx 12/a$  are therefore attenuated by 30 dB or more. The spatial Nyquist wavenumber (the usual condition of two samples per wavelength) is  $k_x(\text{Nyquist}) = 0.5 \times (2\pi/\Delta x)$ . In order to avoid spatial aliasing it is necessary to ensure that  $k_x(\text{max. measured}) < k_x(\text{Nyquist})$  which gives the spatial sampling requirement

$$\Delta x < a\pi/12 \approx a/4. \quad (16)$$

For most types of sensor array, the radius of the sensitive element,  $a$ , is fixed. However, for optically addressed arrays [45, 46] it can sometimes be chosen arbitrarily, thereby allowing control of the spatial anti-aliasing. If, instead of 30 dB, 15 dB attenuation at the Nyquist spatial frequency is considered sufficient to remove spatial aliasing, then requirement (16), which is equivalent to eight measurement points per sensing element diameter, can be reduced to two measurement points per diameter, or  $\Delta x < a$ .

When measurements are made with reflectors in place, the positions of the spatial sampling points with respect to these reflectors is important, to ensure that the samples represent a repeating pattern. The reflectors must be placed a distance  $\Delta x/2$  from the first and last measurements. In other words,  $p(x)$  must be sampled at positions  $(2n + 1)\Delta x/2$ ,  $n = 0, \dots, N - 1$ , giving the measured data  $\{p_0, p_1, \dots, p_{N-1}\}$ , so that these can be made into a repeating sequence by mirroring about  $x = X$ . The data vector for the reconstruction is then  $p_n = \{p_0, \dots, p_{2N-n-1}\}$ , where  $p_{2N-n-1} = p_n$ ,  $n = 0, \dots, N - 1$ . This is illustrated in figure 4.

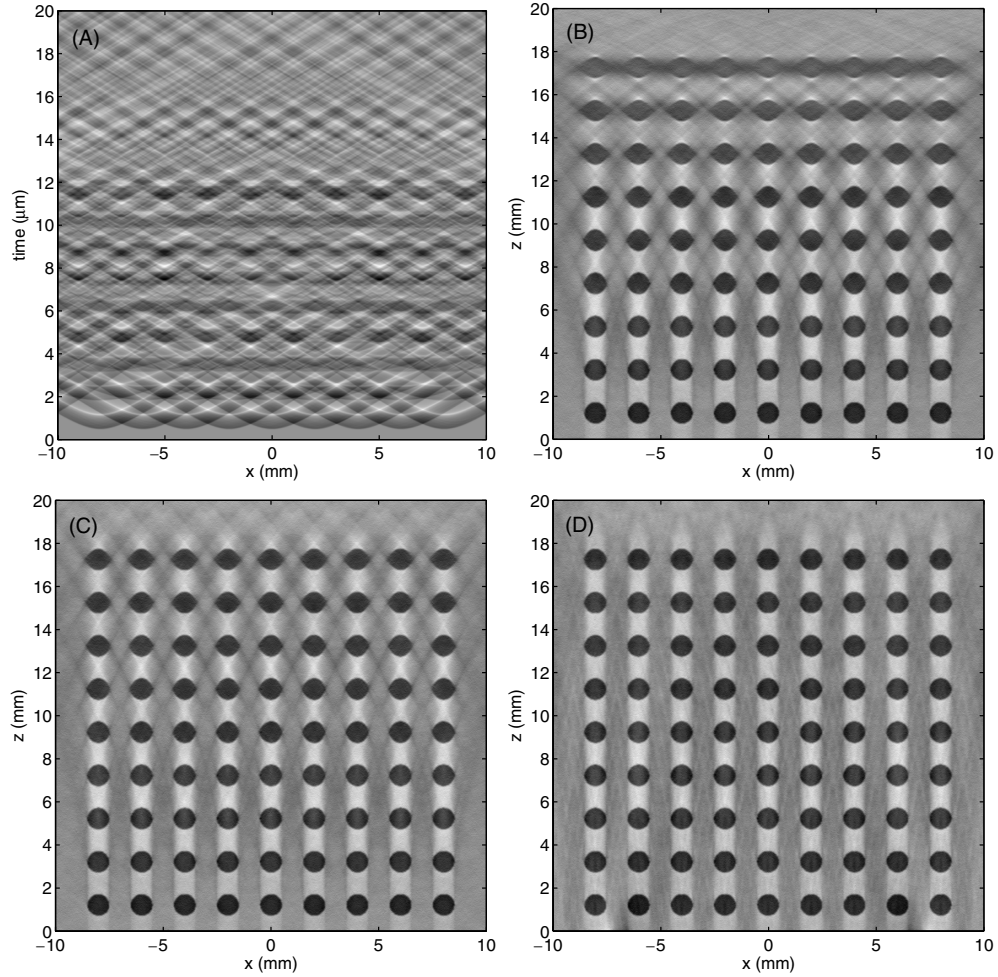


**Figure 5.** (A) Simulated pressure time histories for an array of detectors along the line  $z = 0$ , for a 20 mm aperture,  $-10 \text{ mm} \leqslant x < 10 \text{ mm}$ , bounded by vertical reflectors, and calculated from the initial pressure distribution in figure 2(A) using a k-space algorithm. The reverberation resulting from the reflectors can be seen by comparison with figure 2(B). Images (B)–(D) show estimates of the initial pressure distribution,  $p_{0nm}$ , reconstructed from the pressure time series shown in (A). In (B) time histories from 0 to 14  $\mu\text{s}$  were used, in (C) this was extended to 20  $\mu\text{s}$ , and in (D) to 40  $\mu\text{s}$ , thereby including more of the reverberant energy.

### 3.4. Example using a finite aperture with image sources

Because of the reverberation caused by the vertical reflectors, the pressure time histories will, in theory, continue forever. In practice, however, due to geometric spreading, acoustic absorption, and reflectors with  $|R| < 1$ , the signal will decay to below the noise in a finite length of time. Figures 5(B)–(D) show images reconstructed from the time histories, figure 5(A), which have been simulated from the initial pressure distribution in figure 2(A), although now including the reverberation due to the acoustic reflectors. The data here were simulated using the same  $k$ -space model as for figure 2(B) and the same level of noise is added. Figures 5(B)–(D) used time histories with durations of 14, 20 and 40  $\mu\text{s}$ , respectively.

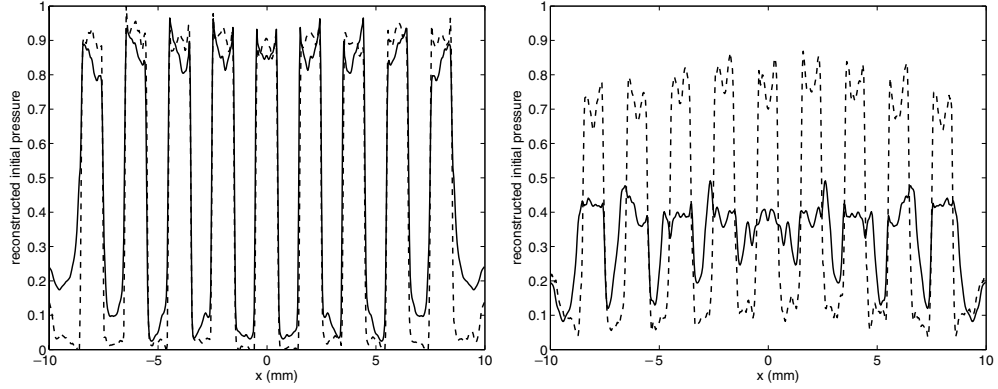


**Figure 6.** Profiles through the bottom row (left) and third from top row (right) of circles in figures 2(F), solid line, and 5(C), dotted line, showing the improvement in the reconstruction further from the sensor when the reverberant data are included.

Figure 6 shows profiles through the bottom row and third from top row of circles in figures 2(F) and 5(C), i.e. with and without reverberant data.

The improvement in the reconstruction from figure 2(F)—the reduction in the artefacts and the considerably reduced blurring—is striking even for short duration data ( $14 \mu\text{s}$  in figure 5(B) compared to  $20 \mu\text{s}$  in figure 2(F)). Three differences between these reconstructions and that of figure 2(F) are apparent. First, while the quality of the reconstruction in figure 2(F) depends on the position in the image (close to the centre of the sensor the image is accurately reconstructed and as one moves further from this point the image quality deteriorates), a different pattern emerges in figures 5(B)–(D). The quality of the reconstruction does not depend on the distance from the centre of the sensor—the circles at each depth are equally well recovered—but only on the distance from the measurement plane, the depth  $z$ . Second, this depth dependence is reduced as more reverberation is used in the reconstruction. Both these features of the image are explained in terms of an ‘effective measurement aperture’ in section 4. Third, artefacts, taking the form of vertical strips aligned with each column of circles, are more clearly visible in figures 5(B)–(D) than in figure 2(F) because of the decreased blurring in the former. These are thought to be due to the fact that the evanescent, non-radiating part of the acoustic spectrum is neglected in the image reconstruction. It is clear from figure 2(C) that there is some energy in the evanescent region of the spectrum of  $P_{kl}$ , e.g. where  $k > (\Delta\omega/c\Delta k_x)l$ , which is lost when interpolating to  $P_{0kq}$ , figure 2(E).

In section 3.3 and figure 4 it is explained that it is necessary that the reflectors are placed a distance  $\Delta x/2$  from the first and last measurement points. When it is not possible for the measurement aperture to extend over the full width of the base of the box, perhaps due to the way the reflectors are fixed to the plane, or because only a sensor array smaller than the box is available, it may still be advantageous to include the reflectors. Figure 8(B) shows an image measured over an aperture which covers only three quarters of the distance between the reflectors, as shown in figure 7. Comparing this to figure 8(A), which was generated using the same set-up and reconstruction algorithm, but without the reverberation due to the reflectors, it is clear that there is some advantage still to be had by including the reflectors. Whilst there are artefacts in figure 8(B), the edges of many of the circles are recovered much more satisfactorily. The reason that this is so can be understood using the concept of the ‘effective measurement aperture’.

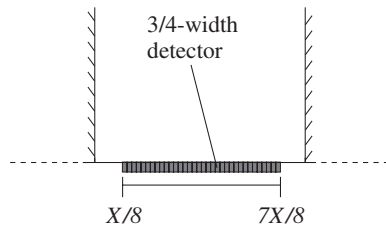


**Figure 7.** The 3/4-width aperture used to reconstruct the images in figure 8.

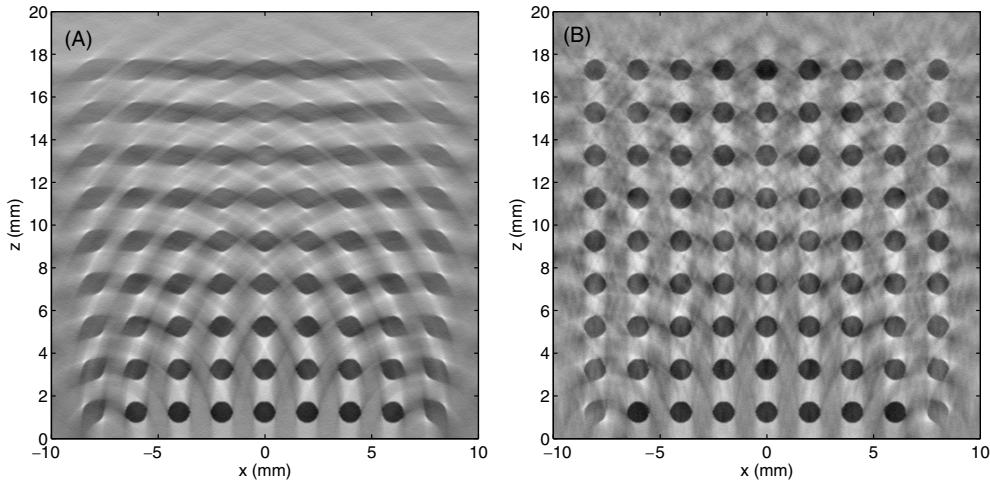


**Figure 8.** Images reconstructed using the data from a 3/4-width aperture (figure 7), (A) without reflectors, (B) with reflectors.

#### 4. Effective measurement aperture

Many imaging targets of interest will contain sharp boundaries delimiting regions of different contrast, such as is the case with the circles in figure 2(A) or, for instance, blood vessels in tissue. In order to reconstruct the shapes of these regions accurately, the imaging scheme must be able to reconstruct the boundaries—*i.e.*, where the contrast changes rapidly over a short distance. The Louis–Quinto theorem, a result from microlocal analysis of the spherical mean Radon transform due to Louis and Quinto [7], but quoted here from Anastasio and Zhang [47], states:

*A boundary located at position  $\mathbf{x}$  can be reconstructed stably if and only if one of the two normal directions to the boundary at  $\mathbf{x}$  intersects the measurement surface.*

A boundary that can, in principle, be reconstructed stably *i.e.*, accurately without blurring, is called ‘visible’. The accuracy with which a visible boundary is actually reconstructed depends on the particular reconstruction algorithm used. Boundaries that cannot be reconstructed stably even in principle are called ‘invisible’, and usually appear smoothed. This result highlights a problem with finite width planar apertures. For an *infinitely wide* planar aperture, where a normal to every conceivable boundary must cross the measurement surface somewhere, all the boundaries in the image can be stably reconstructed, but using data from an array with

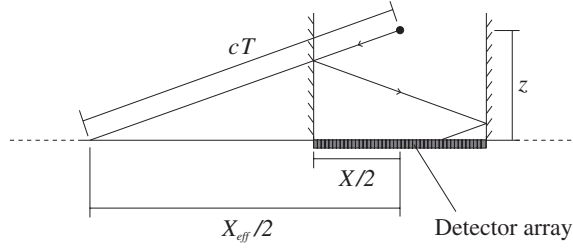


**Figure 9.** The effective aperture width  $X_{\text{eff}}$  is governed by the time over which the reverberation is recorded  $t$ , rather than the actual width  $X$  of the detector. It is also dependent on the height of the source  $z$  above the detector plane.

a finite-aperture means that some of the boundaries cannot be reconstructed. However, it is clear, by comparing figures 2(F) and 5(D), that by including the reflectors, the boundaries, i.e. the edges of the circles, have been reconstructed more accurately. This is so even though the side walls are not *per se* part of the measurement array, which consists of just the planar surface perpendicular to, and between, the reflectors. Adding the reflectors appears to increase the width of the measurement aperture in some sense, thus allowing the boundaries to be reconstructed more accurately. In this section, an intuitive definition of ‘effective measurement aperture’ is proposed and whether or not it acts as a measurement surface in the sense of the Louis–Quinto theorem is investigated.

The ‘effective measurement aperture’, or simply ‘effective aperture’, is defined for a point at  $(x, z)$  as the region in the plane  $z = 0$  for which the distance from  $(x, z)$  to the plane is less than or equal to  $cT$ , as shown in figure 9, where  $T$  is the duration of the measurements. Some simple trigonometry shows that the ‘effective’ aperture width is given by  $X_{\text{eff}} = 2\sqrt{(cT)^2 - z^2}$ . This expression for the effective aperture width shows that for  $z \ll cT$ , doubling the length of time over which the reverberation is recorded doubles the effective aperture. Also, the angle  $\theta$  subtended by an actual aperture of width  $X$  at a height  $z$  is given by  $\tan(\theta/2) = X/(2z)$ , whereas the angle  $\theta_{\text{eff}}$  subtended by the effective aperture is given by  $\tan(\theta_{\text{eff}}/2) = \sqrt{(cT/z)^2 - 1}$ .

To show that the ‘effective measurement aperture’ acts as a measurement surface in the Louis–Quinto sense, it is necessary to determine that when the normal to a boundary at a point  $x_0$  crosses the ‘effective measurement aperture’—even if not the actual sensing area—the boundary at  $x_0$  is stably reconstructed.  $|\nabla h_{np}|$ , the magnitude of the discrete gradient, is used as an indicator of how well the boundaries in the image have been reconstructed. Figure 10 shows a plot of the magnitude of the gradient of figure 5(B), which was reconstructed from measurements made over  $14 \mu\text{s}$ . Superimposed on the plot are lines showing the angle subtended by the effective measurement apertures, as illustrated in figure 9, for three of the circles in the image. While there are no clear cut-off points between where a boundary is well recovered and where it is poorly recovered, nevertheless, there is clearly good agreement between those parts of the boundary that have been recovered with a large gradient, and therefore stably, and those parts of the boundary whose normals lie in between the two lines bounding the angle subtended by the effective measurement aperture. (This short-time-history example was chosen so that the effective aperture was narrow enough to be displayed easily. In addition, the boundaries in images figures 5(C) and (D) were so well recovered that the plot of the gradient varied little from circle to circle.)

For comparison, figure 11 shows a plot of the magnitude of the gradient of figure 2(F) in the case where the reverberant data are not included. Superimposed on this image are lines

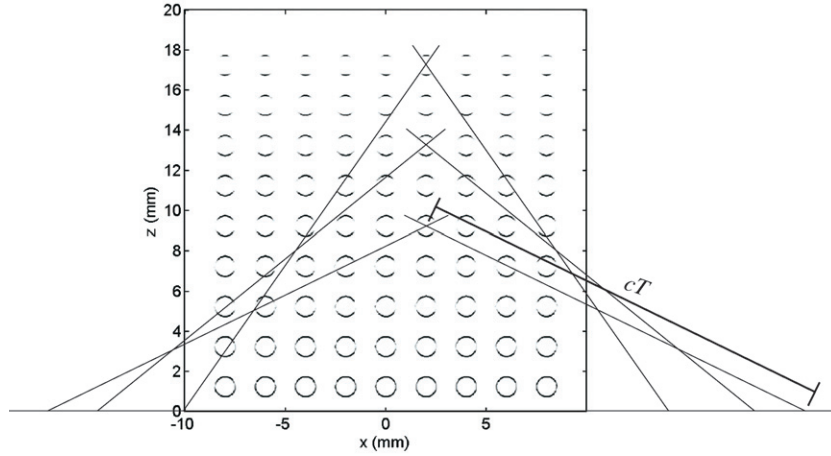


**Figure 10.** The magnitude of the gradient of the image shown in figure 5(B), reconstructed from  $14 \mu\text{s}$  time histories, including the reverberation due to the reflectors. Radial lines marking out the ‘effective measurement aperture’ have been superimposed. The boundaries of the circles in the image can be visibly reconstructed within the angle subtended by the *effective* aperture.

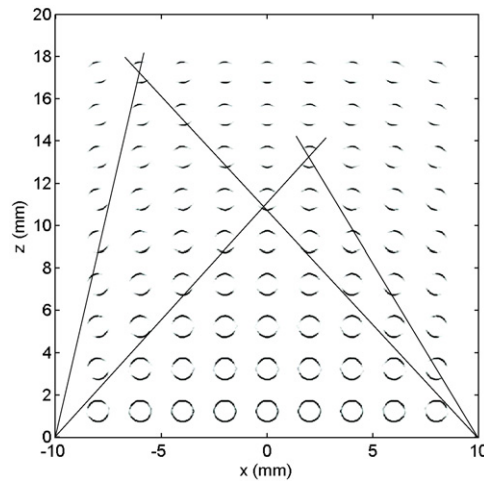


**Figure 11.** The magnitude of the gradient of the image shown in figure 2(F). Radial lines marking out the angle subtended by the sensor have been superimposed. The boundaries of the circles in the image can be visibly reconstructed within the angle subtended by the aperture.

showing the angles subtended by the actual measurement aperture. The boundaries that lie within the angle defined by the actual measurement aperture are recovered stably, in agreement with the Louis–Quinto theorem. It is also clear now why the image quality in figures 5(B)–(D) does not depend on position in the same way as figure 2(F). Every point in figures 10 is in the centre of its effective measurement aperture, whereas only the points on the line  $x = 0$  are in the centre of the actual measurement aperture in figure 11. The other points lie either one side or the other of this line, leading to an asymmetry in the measurements and thus asymmetry in the distortion of the image.

## 5. Discussion

The main advantage of introducing image sources by using acoustic reflectors perpendicular to the planar sensor—the improvement in the image quality due to the reduction of blurring and artefacts—has been described above. In this section some of the other advantages, practicalities, and applications of such a system are discussed.

One difference between planar imaging with and without reflectors, is that in the former case the object to be imaged must fit between the reflectors. This still allows a wide range of potential uses, including breast imaging, whole body imaging of small animals, and imaging of *ex vivo* tissue samples. Monitoring the growth of engineered tissue and, perhaps, plant morphology may also be possible.

### 5.1. Temporal versus spatial measurements

There are two related points here. The first is that small arrays are often preferable to large arrays, due to reasons of technical complexity and cost. The second concerns the efficiency of data storage. Consider a 2D detector array consisting of  $N \times N$  equally spaced elements. Doubling the aperture of this array in both directions will require a  $2N \times 2N$  array, a four-fold increase in the number of individual elements. By using reflectors with the smaller array, however, it has been shown that it is possible to achieve an effective aperture size similar to the larger array simply by recording the reverberant data for twice as long. The increased technical complexity of making measurements over a larger array, and the much greater cost, can therefore be avoided. For measurements over a 2D surface, the number of data recorded is  $N^2 \times M$ , where  $M$  is the number of samples in time. It was noted in section 4 that doubling the duration of the measurement, doubling  $M$ , is equivalent to doubling  $N$  when  $z \ll ct$ . Doubling the measurement aperture in both dimensions leads to four times as much data,  $(2N)^2 \times M$ , but doubling the duration of the measurement gives only twice as much,  $N^2 \times (2M)$ . For high resolution images, which require a large number of sampling points, this saving of a factor of two in the storage requirement may be beneficial. The reverberant-field data carry the information on the source distribution more efficiently than the free-field data.

### 5.2. Point spread function deblurring

One way to improve an image such as figure 2(F) is to deblur the image using knowledge of the point spread function (PSF) of the imaging system. The point spread function will consist of two parts, one due to the nature of the detector and the other due to the finite measurement aperture. The first part is often spatially invariant, but the effect of the finite aperture on the PSF is to introduce considerable spatial variation. It is this variation that causes the spatially dependent blurring in figure 2(F).

Imaging with image sources results in a PSF that is independent of  $x$ ; recording over a sufficiently long time duration also reduces the spatial dependence on  $z$ , resulting in a PSF that is essentially spatially independent, as shown in figure 5(D). This is significant, for it is considerably easier to deconvolve a spatially independent PSF from an image than it is to deblur using a spatially dependent one.

### 5.3. Model assumptions

Several of the assumptions made in deriving the image reconstruction algorithm will be met only approximately in practical implementations. In particular, the sound speed will never be exactly uniform in tissue, acoustic absorption will attenuate the signal to some extent, and

the reflectors will not be perfectly reflecting. Sound speed heterogeneities within the sample will make the later-arriving reflections less useful in the image reconstruction than the early arrivals, because of the accumulated phase distortion from having travelled a greater distance through the heterogeneous sample. However, both the acoustic absorption and the less-than-perfectly reflecting reflectors will dampen the reverberant signal so that it will fall into the noise sooner than it would otherwise, and will therefore act to reduce the effect of these later arrivals on the image. It was shown in figure 5 that even using just the first few reflections can improve the resolution of the image considerably.

A model-based photoacoustic image reconstruction scheme that uses reverberant data from an arbitrarily shaped reverberant cavity, and can take into account non-perfect reflectors, sound speed heterogeneities, and so on, is conceivable but it would lack the simplicity and efficiency of the method described here, and would not provide the same level of insight into the reconstruction problem.

## 6. Conclusions

A technique for PAT without finite aperture effects has been described. Acoustic reflectors, placed at either end of the finite aperture sensor and perpendicular to it, introduce acoustic image sources which make the acoustic field spatially periodic. By exploiting the periodicity inherently assumed by the discrete Fourier transform, an existing and efficient method for reconstructing PAT images from planar measurements can be used to reconstruct images exactly from the measured reverberant field. This technique allows the acoustic data emitted over a solid angle approaching  $2\pi$  steradians to be measured, whilst maintaining the planar measurement geometry for which there exists an efficient reconstruction algorithm.

There are a number of benefits of this planar approach over circular, cylindrical and spherical geometries: planar sensor arrays (including optically-addressed arrays) are readily available, a large and therefore expensive array is not required for high resolution imaging, the image reconstruction is exact and efficient, and the PSF of the sensor can be deconvolved straightforwardly from these images, improving the image quality still further. These advantages offer the prospect of rapidly acquired photoacoustic images with high, spatially invariant resolution.

## Acknowledgment

This work was supported by the EPSRC, UK.

## References

- [1] de Mul F F M and Hoelen C G A 1998 Three-dimensional imaging of blood vessels in tissue using photoacoustics *J. Vas. Res.* **35** 192
- [2] Hoelen C G A, de Mul F F M, Pongers R and Dekker A 1998 Three-dimensional photoacoustic imaging of blood vessels in tissue *Opt. Lett.* **23** 648–50
- [3] Zhang E Z, Laufer J G and Beard P C 2007 Three-dimensional photoacoustic imaging of vascular anatomy in small animals using an optical detection system *Proc. SPIE* **6437** 64370S
- [4] Kruger R A, Reynolds H E, Kiser W, Reinecke D R and Kruger G A 1999 Thermoacoustic computed tomography for breast imaging *Radiology* **210** K06H
- [5] Oraevsky A A, Savateeva E V, Solomatin S V, Karabutov A, Andreev V G, Gatalica Z, Khamapirad T and Henrichs P M 2002 Optoacoustic imaging of blood for visualization and diagnostics of breast cancer *Proc. SPIE* **4618** 461881
- [6] Wang X, Pang Y, Ku G, Xie X, Stoica G and Wang L V 2003 Noninvasive laser-induced photoacoustic tomography for structural and functional *in vivo* imaging of the brain *Nature Biotech.* **21** 803–6

- [7] Louis A K and Quinto E T 2000 Local tomographic methods in sonar *Surveys on Solution Methods for Inverse Problems* (Vienna: Springer) pp 147–54
- [8] Cox B T, Arridge S R, Köstli K and Beard P C 2006 2D quantitative photoacoustic image reconstruction of absorption distributions in scattering media using a simple iterative method *Appl. Opt.* **45** 1866–74
- [9] Cox B T, Arridge S R and Beard P C 2007 Gradient-based quantitative photoacoustic image reconstruction for molecular imaging *Proc. SPIE* **6437** 64371T
- [10] Norton S J and Linzer M 1981 Ultrasonic reflectivity imaging in three dimensions—exact inverse scattering solutions for plane, cylindrical and spherical apertures *IEEE Trans. Biomed. Eng.* **28** 202–20
- [11] Xu M H and Wang L H V 2002 Time-domain reconstruction for thermoacoustic tomography in a spherical geometry *IEEE Trans. Med. Imag.* **21** 814–22
- [12] Finch D, Patch S K and Rakesh 2003 Determining a function from its mean values over a family of spheres *SIAM J. Math. Anal.* **35** 1213–40
- [13] Kunyansky L A 2007 Explicit inversion formulae for the spherical mean Radon transform *Inverse Problems* **23** 373–83
- [14] Xu Y, Xu M H and Wang L H V 2002 Exact frequency-domain reconstruction for thermoacoustic tomography: II. Cylindrical geometry *IEEE Trans. Med. Imag.* **21** 829–33
- [15] Norton S J and Vo-Dinh T 2003 Optoacoustic diffraction tomography: analysis of algorithms *J. Opt. Soc. Am. A* **20** 1859–66
- [16] Köstli K P, Frenz M, Bebie H and Weber H P 2001 Temporal backward projection of optoacoustic pressure transients using Fourier transform methods *Phys. Med. Biol.* **46** 1863–72
- [17] Xu Y, Feng D Z and Wang L H V 2002 Exact frequency-domain reconstruction for thermoacoustic tomography: I. Planar geometry *IEEE Trans. Med. Imag.* **21** 823–8
- [18] Jiang H, Yuan Z and Gu X 2006 Spatially varying optical and acoustic property reconstruction using finite-element-based photoacoustic tomography *J. Opt. Soc. Am.* **23** 878–88
- [19] Kruger R A, Liu P, Fang Y R and Appledorn C R 1995 Photoacoustic ultrasound (PAUS)—reconstruction tomography *Med. Phys.* **22** 1605–9
- [20] Liu P Y 1998 The P-transform and photoacoustic image reconstruction *Phys. Med. Biol.* **43** 667–74
- [21] Kruger R A, Reinecke D R and Kruger G A 1999 Thermoacoustic computed tomography—technical considerations *Med. Phys.* **26** 1832–7
- [22] Hoelen C G A and de Mul F F M 2000 Image reconstruction for photoacoustic scanning of tissue structures *Appl. Opt.* **39** 5872–83
- [23] Zhulina Y V 2000 Optimal statistical approach to optoacoustic image reconstruction *Appl. Opt.* **39** 5971–7
- [24] Köstli K P, Frenz M, Weber H P, Paltauf G and Schmidt-Kloiber H 2001 Optoacoustic tomography: time-gated measurement of pressure distributions and image reconstruction *Appl. Opt.* **40** 3800–9
- [25] Paltauf G, Viator J A, Prahl S A and Jacques S L 2002 Iterative reconstruction algorithm for optoacoustic imaging *J. Acoust. Soc. Am.* **112** 1536–44
- [26] Xu M H, Xu Y and Wang L H V 2003 Time-domain reconstruction-algorithms and numerical simulations for thermoacoustic tomography in various geometries *IEEE Trans. Biomed. Eng.* **50** 1086–99
- [27] Xu Y and Wang L V 2004 Time reversal and its application to tomography with diffracting sources *Phys. Rev. Lett.* **92** 033902
- [28] Xu M and Wang L V 2005 Universal back-projection algorithm for photoacoustic computed tomography *Phys. Rev. E* **71** 016706
- [29] Zhang J, Anastasio M A, Pan X and Wang L V 2005 Weighted expectation maximization reconstruction algorithms for thermoacoustic tomography *IEEE Trans. Med. Imag.* **24** 817–20
- [30] Xu M and Wang L V 2006 Photoacoustic imaging in biomedicine *Rev. Sci. Instrum.* **77** 041101
- [31] Zhang E Z and Beard P C 2006 2D backward-mode photoacoustic imaging system for NIR (650–1200 nm) spectroscopic biomedical applications *Proc. SPIE* **6086** 60860H
- [32] Anastasio M A, Zhang J, Pan X, Zou Y, Ku G and Wang L V 2005 Half-time image reconstruction in thermoacoustic tomography *IEEE Trans. Med. Imag.* **24** 199–210
- [33] Stolt R H 1978 Migration by Fourier transform *Geophysics* **43** 23–48
- [34] Cohen J K and Bleistein N 1979 Velocity inversion procedure for acoustic waves *Geophysics* **44** 1077–87
- [35] Nagai K 1985 A new synthetic-aperture focusing method for ultrasonic B-scan imaging by the Fourier transform *IEEE Trans. Son. Ultrason.* **SU-32** 531–6
- [36] Cafforio C, Prati C and Rocca E 1991 SAR data focusing using seismic migration techniques *IEEE Trans. Aerosp. Electron. Syst.* **27** 194–207
- [37] Fawcett J A 1985 Inversion of  $N$ -dimensional spherical averages *SIAM J. Appl. Math.* **45** 336–41
- [38] Andersson L-E 1988 On the determination of a function from spherical averages *SIAM J. Math. Anal.* **19** 214–32

- [39] Köstli K P and Beard P C 2003 Two-dimensional photoacoustic imaging by use of Fourier-transform image reconstruction and a detector with an anisotropic response *Appl. Opt.* **42** 1899–908
- [40] Cox B T and Beard P C 2005 Fast calculation of pulsed photoacoustic fields in fluids using *k*-space methods *J. Acoust. Soc. Am.* **117** 3616–27
- [41] Tabei M, Mast T D and Waag R C 2002 A *k*-space method for coupled first-order acoustic propagation equations *J. Acoust. Soc. Am.* **111** 53–63
- [42] Cox B T and Beard P C 2007 *k*-space propagation models for acoustically heterogeneous media: application to biomedical photoacoustics *J. Acoust. Soc. Am.* **121** 3453–64
- [43] Xu Y, Wang L V, Ambartsoumian G and Kuchment P 2004 Reconstructions in limited-view thermoacoustic tomography *Med. Phys.* **31** 724–33
- [44] Cox B T and Beard P C 2007 Exact photoacoustic image reconstruction using a planar sensor array and image sources *Proc. SPIE* **6437** 64371H
- [45] Beard P C 2005 2D ultrasound receive array using an angle-tuned Fabry Perot polymer film sensor for transducer field characterisation and transmission ultrasound imaging *IEEE Trans.UFFC* **52** 1002–12
- [46] Zhang E Z and Beard P C 2006 Broadband ultrasonic field mapping system using a wavelength tuned, optically scanned focussed beam to interrogate a Fabry–Perot polymer film sensor *IEEE Trans. UFFC* **53** 1330–8
- [47] Anastasio M A and Zhang J 2006 Image reconstruction in photoacoustic tomography with truncated cylindrical measurement apertures *Proc. SPIE* **6086** 608610